4828 *Inorg. Chem.* **2009,** *48,* 4828–4836
DOI:10.1021/ic900001y

Inorganic Chemistry
Article

Iron(II) Complexes with Redox-Active Tetrazene (RNNNNR) Ligands

Ryan E. Cowley,[†] Eckhard Bill,[*,‡] Frank Neese,[*,§] William W. Brennessel,[†] and Patrick L. Holland[*,†]

[†]*Department of Chemistry, University of Rochester, Rochester, New York 14627,* [‡]*Max-Planck-Institut für Bioanorganische Chemie, Mülheim an der Ruhr, Germany, and* [§]*Institut für Physikalische and Theoretische Chemie, Universität Bonn, Bonn, Germany*

Received January 1, 2009

This paper describes the redox chemistry of a tetrazene ligand on (β-diketiminato)iron complexes. Addition of 1-adamantyl azide to an iron(I) source gives the tetrazene complex $L^{Me}Fe(AdNNNNAd)$, most likely through an imidoiron(III) intermediate. Spectroscopic, magnetic, crystallographic, and computational investigations of the tetrazene complex show that one unpaired spin occupies a primarily ligand-based orbital, and is antiferromagnetically coupled to a high-spin iron(II) ion to give an $S = 3/2$ ground state. Reversible single-electron reduction occurs at the ligand singly occupied molecular orbital (SOMO), affording a dianionic tetrazene ligand while leaving the metal oxidation state and spin state unchanged.

Introduction

There is great interest in ligands that display "non-innocent behavior" by virtue of their ability to donate or accept variable amounts of charge from a metal.[1−4] While redox non-innocence can enable novel reactions, it also introduces ambiguities to the assignment of an oxidation state to the metal, which is a research challenge. The most intensively studied non-innocent ligands are those that give a five-membered chelate ring, exemplified by α-diimine and dithiolene.[4] Recent work by Wieghardt and co-workers has used a combination of advanced spectroscopic techniques and quantum chemical calculations to unambiguously determine the oxidation level of the metal and ligand in complexes of a number of metals.[4] Typically, the ligand radical is strongly coupled ($-J > 300\ cm^{-1}$) to the nearby metal center, and the metal and ligand can exchange charge easily. Because of the ability of redox-active ligands to act as electron reservoirs for use in reduction and oxidation reactions, a growing number of redox non-innocent ligands have been explored.[1−3]

There has not been much study of the redox activity of tetrazene (RNNNNR) ligands, which are isoelectronic with dithiolenes and α-diimines.[5] Pioneering work by Trogler and others originally described tetrazenes as strong π-acceptors[6] capable of facilitating dissociative ligand substitution[7] or photochemical N_2 extrusion,[8] and capable of supporting 19-electron complexes in solution.[9] However, assigning the oxidation state of the metal and tetrazene ligand in such a complex is not immediately clear. The RNNNNR fragment (Figure 1) can be described as a neutral ligand (**A**), a dianion (**C**), or the monoanionic radical (**B**).

The redox assignments of the few odd-electron tetrazene complexes in the literature have been somewhat ambiguous and qualitative. For example, electron paramagnetic resonance (EPR) studies of $[CpCo(RNNNNR)]^-$ (R = Me, Ph, C_6F_5, 2,4-$F_2C_6H_3$, 2,6-$Me_2C_6H_3$) suggested that the radical occupies a molecular orbital (MO) with about 60% Co(3d) character.[9] The EPR spectrum of $[Mo(PhNNNNPh)(CO)_2(PEt_3)_2]^-$ showed significant hyperfine coupling to Mo, consistent with a radical with some metal-based character.[10] The presence of a N(1s) shakeup satellite in the X-ray photoelectron spectroscopy (XPS) spectrum of CpNi(TolNNNNTol) (Tol = *p*-tolyl) indicated possible delocalization of the radical onto the tetrazene ligand, although hyperfine coupling to only two of the nitrogen atoms suggested that the radical lies mainly on the metal.[11]

Iron complexes offer the opportunity to use Mössbauer spectroscopy to establish the metal's oxidation state,[12] giving a more firm conclusion as to electron location. Although the first crystallographically characterized tetrazene complex was the iron complex $Fe(CO)_3$(MeNNNNMe) in 1968,[13] no other iron tetrazene complexes were structurally characterized until a paper from Riordan and co-workers in 2008.[14] In this work, we use crystallography, magnetism, EPR, and Mössbauer spectroscopy to characterize an iron-tetrazene

* To whom correspondence should be addressed. E-mail: holland@chem.rochester.edu.

(1) (a) Wang, K.; Stiefel, E. I. *Science* **2001**, *291*, 106–109. (b) Harrison, D. J.; Nguyen, N.; Lough, A. J.; Fekl, U. *J. Am. Chem. Soc.* **2006**, *128*, 11026–11027.

(2) (a) Haneline, M. R.; Heyduk, A. F. *J. Am. Chem. Soc.* **2006**, *128*, 8410–8411. (b) Blackmore, K. J.; Lal, N.; Ziller, J. W.; Heyduk, A. F. *J. Am. Chem. Soc.* **2008**, *130*, 2728–2729.

(3) (a) Adhikari, D.; Mossin, S.; Basuli, F.; Huffman, J. C.; Szilagyi, R. K.; Meyer, K.; Mindiola, D. J. *J. Am. Chem. Soc.* **2008**, *130*, 3676–3682. (b) Trovitch, R. J.; Lobkovsky, E.; Chirik, P. J. *Inorg. Chem.* **2006**, *45*, 7252–7260. (c) Bouwkamp, M. W.; Bowman, A. C.; Lobkovsky, E.; Chirik, P. J. *J. Am. Chem. Soc.* **2006**, *128*, 13340–13341.

Published on Web 4/27/2009

complex as a tetrazene radical anion (**B**) with strong magnetic coupling to an iron(II) center. Additionally, the redox activity of the tetrazene unit is demonstrated via one-electron reduction of the complex at the tetrazene ligand. Computational studies are used to support and illuminate the proposed electronic structures of the complexes.

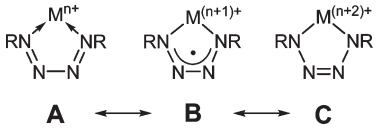

Figure 1. Formal electronic configurations for a tetrazene ligand.

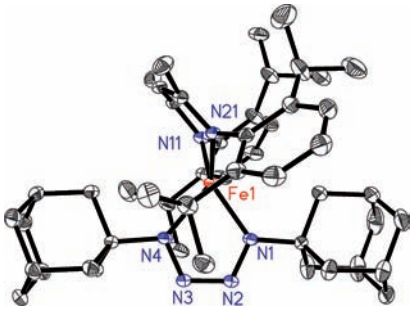

Figure 2. Molecular structure of $L^{Me}Fe(AdNNNNAd)$ (**1**), using 50% probability thermal ellipsoids. Selected bond distances [Å]: Fe1−N1, 1.953(2); Fe1−N4, 2.042(2); N1−N2, 1.317(2); N2−N3, 1.334 (2); N3−N4, 1.309(2); Fe1−N11, 1.996(2); Fe1−N21, 1.991(2).

Scheme 1. Formation of Tetrazene Complex **1**

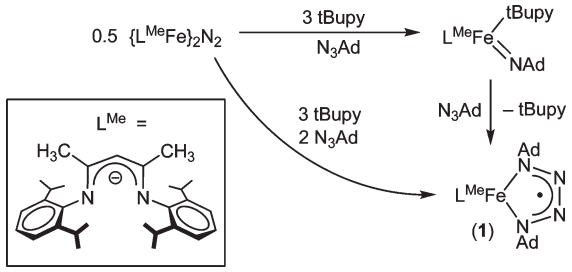

Results and Discussion

Synthesis and Structure. When excess 1-azidoadamantane (N_3Ad) is added to a solution of the formally iron(I) dinitrogen complex $L^{Me}FeNNFeL^{Me}$ (L^{Me} = $HC[C(Me)N(2,6\text{-}iPr_2C_6H_3)]_2$),[15] then the unusual hexazene complex $\{L^{Me}Fe\}_2(\mu\text{-}AdN_6Ad)$ is isolated, as we reported recently.[16] However, the outcome of the reaction is different in the presence of excess 4-*tert*-butylpyridine (tBupy). Sequential addition of 6 equiv of tBupy (3 equiv per iron) and 4 equiv of N_3Ad (2 equiv per iron) to a pentane solution of $L^{Me}FeNNFeL^{Me}$ gives an olive-green precipitate in 81% yield (Scheme 1). The molecular structure of the green product was determined by single-crystal X-ray diffraction (Figure 2) to be $L^{Me}Fe(AdNNNNAd)$ (**1**).

Complex **1** contains 1,4-bis(adamantyl)tetrazene and diketiminate ligands coordinated to a pseudotetrahedral iron center (the twist angle between the N11−Fe−N21 and N1−Fe−N4 planes is 89.28(6)°). The iron atom resides 0.855(2) Å out of the N_2C_3 plane of the diketiminate, and the tetrazene ligand is pushed toward one face of the diketiminate. This conformation presumably arises from the need to avoid steric congestion between the isopropyl groups of L^{Me} and the adamantyl moieties of the tetrazene ligand. This distortion is also manifested in Ga and Al tetrazene complexes supported by L^{Me}.[17,18] The ^1H NMR spectrum of **1** suggests that the pseudo-C_s symmetry of the crystal structure is retained in solution.

(4) (a) De Bruin, B.; Bill, E.; Bothe, E.; Weyhermüller, T.; Wieghardt, K. *Inorg. Chem.* **2000**, *39*, 2936–2947. (b) Dutta, S. K.; Beckmann, U.; Bill, E.; Weyhermüller, T.; Wieghardt, K. *Inorg. Chem.* **2000**, *39*, 3355–3364. (c) Chun, H.; Verani, C. N.; Chaudhuri, P.; Bothe, E.; Bill, E.; Weyhermüller, T.; Wieghardt, K. *Inorg. Chem.* **2001**, *40*, 4157–4166. (d) Chun, H.; Weyhermüller, T.; Bill, E.; Wieghardt, K. *Angew. Chem., Int. Ed.* **2001**, *40*, 2489–2492. (e) Bachler, V.; Olbrich, G.; Neese, F.; Wieghardt, K. *Inorg. Chem.* **2002**, *41*, 4179–4193. (f) Sun, X.; Chun, H.; Hildenbrand, K.; Bothe, E.; Weyhermüller, T.; Neese, F.; Wieghardt, K. *Inorg. Chem.* **2002**, *41*, 4295–4303. (g) Ghosh, P.; Begum, A.; Bill, E.; Weyhermüller, T.; Wieghardt, K. *Inorg. Chem.* **2003**, *42*, 3208–3215. (h) Ghosh, P.; Begum, A.; Herebian, D.; Bothe, E.; Hildenbrand, K.; Weyhermüller, T.; Wieghardt, K. *Angew. Chem., Int. Ed.* **2003**, *42*, 563–567. (i) Ghosh, P.; Bill, E.; Weyhermüller, T.; Wieghardt, K. *J. Am. Chem. Soc.* **2003**, *125*, 3967–3979. (j) Min, K. S.; Weyhermüller, T.; Wieghardt, K. *Dalton Trans.* **2003**, 1126–1132. (k) Ray, K.; Weyhermüller, T.; Goossens, A.; Crajé, M. W. J.; Wieghardt, K. *Inorg. Chem.* **2003**, *42*, 4082–4087. (l) Chlopek, K.; Bill, E.; Ueller, T. W.; Wieghardt, K. *Inorg. Chem.* **2005**, *44*, 7087–7098. (m) Blanchard, S.; Neese, F.; Bothe, E.; Bill, E.; Weyhermüller, T.; Wieghardt, K. *Inorg. Chem.* **2005**, *44*, 3636–3656. (n) Kokatam, S.; Weyhermüller, T.; Bothe, E.; Chaudhuri, P.; Wieghardt, K. *Inorg. Chem.* **2005**, *44*, 3709–3717. (o) Ray, K.; Begum, A.; Weyhermüller, T.; Piligkos, S.; Van Slageren, J.; Neese, F.; Wieghardt, K. *J. Am. Chem. Soc.* **2005**, *127*, 4403–4415. (p) Ray, K.; Bill, E.; Weyhermüller, T.; Wieghardt, K. *J. Am. Chem. Soc.* **2005**, *127*, 5641–5654. (q) Ray, K.; Weyhermüller, T.; Neese, F.; Wieghardt, K. *Inorg. Chem.* **2005**, *44*, 5345–5360. (r) Patra, A. K.; Bill, E.; Weyhermüller, T.; Stobie, K.; Bell, Z.; Ward, M. D.; McCleverty, J. A.; Wieghardt, K. *Inorg. Chem.* **2006**, *45*, 6541–6548. (s) Petrenko, T.; Ray, K.; Wieghardt, K. E.; Neese, F. *J. Am. Chem. Soc.* **2006**, *128*, 4422–4436. (t) Szilagyi, R. K.; Lim, B. S.; Glaser, T.; Holm, R. H.; Hedman, B.; Hodgson, K. O.; Solomon, E. I. *J. Am. Chem. Soc.* **2003**, *125*, 9158–9169. (u) Ray, K.; Petrenko, T.; Wieghardt, K.; Neese, F. *Dalton Trans.* **2007**, 1552–1566. (v) Bill, E.; Bothe, E.; Chaudhuri, P.; Chlopek, K.; Herebian, D.; Kokatam, S.; Ray, K.; Weyhermüller, T.; Neese, F.; Wieghardt, K. *Chem. Eur. J.* **2005**, *11*, 204–224.

(5) (a) Carty, A. J. *Organomet. Chem. Rev. A* **1972**, *7*, 191–243. (b) Haiduc, I.; Silaghi-Dumitrescu, I. *Coord. Chem. Rev.* **1986**, *74*, 127–270. (c) Moore, D. S.; Robinson, S. D. *Adv. Inorg. Chem.* **1986**, *30*, 1–68.

(6) (a) Trogler, W. C.; Johnson, C. E.; Ellis, D. E. *Inorg. Chem.* **1981**, *20*, 980–986. (b) Gross, M. E.; Trogler, W. C.; Ibers, J. A. *J. Am. Chem. Soc.* **1981**, *103*, 192–193. (c) Johnson, C. E.; Trogler, W. C. *J. Am. Chem. Soc.* **1981**, *103*, 6352–6358. (d) Gross, M. E.; Trogler, W. C.; Ibers, J. A. *Organometallics* **1982**, *1*, 732–739. (e) Overbosch, P.; Van Koten, G.; Overbeek, O. *Inorg. Chem.* **1982**, *21*, 2373–2378.

(7) Chang, C.-Y.; Johnson, C. E.; Richmond, T. G.; Chen, Y.-T.; Trogler, W. C.; Basolo, F. *Inorg. Chem.* **1981**, *20*, 3167–3172.

(8) (a) Gross, M. E.; Trogler, W. C. *J. Organomet. Chem.* **1981**, *209*, 407–414. (b) Gross, M. E.; Johnson, C. E.; Maroney, M. J.; Trogler, W. C. *Inorg. Chem.* **1984**, *23*, 2968–2973.

(9) Maroney, M. J.; Trogler, W. C. *J. Am. Chem. Soc.* **1984**, *106*, 4144–4151.

(10) Lee, S. W.; Trogler, W. C. *Organometallics* **1990**, *9*, 1470–1478.

(11) Overbosch, P.; Van Koten, G.; Spek, A. L.; Roelofsen, G.; Duisenberg, A. J. M. *Inorg. Chem.* **1982**, *21*, 3908–3913.

(12) Münck, E. Aspects of ^{57}Fe Mössbauer Spectroscopy. In *Physical Methods in Bioinorganic Chemistry*; L., Que, Jr., Ed.; University Science Books: Sausalito, CA, 2000.

(13) Doedens, R. J. *Chem. Commun.* **1968**, 1271–1272. See also: Dekker, M.; Knox, G. R. *Chem. Commun.* **1967**, 1243–1244.

(14) Mock, M. T.; Popescu, C. V.; Yap, G. P. A.; Dougherty, W. G.; Riordan, C. G. *Inorg. Chem.* **2008**, *47*, 1889–1891.

(15) Smith, J. M.; Sadique, A. R.; Cundari, T. R.; Rodgers, K. R.; Lukat-Rodgers, G.; Lachicotte, R. J.; Flaschenriem, C. J.; Vela, J.; Holland, P. L. *J. Am. Chem. Soc.* **2006**, *128*, 756–769.

(16) Cowley, R. E.; Elhaïk, J.; Eckert, N. A.; Brennessel, W. W.; Bill, E.; Holland, P. L. *J. Am. Chem. Soc.* **2008**, *130*, 6074–6075.

(17) Hardman, N. J.; Power, P. P. *Chem. Commun.* **2001**, 1184–1185.

(18) Zhu, H.; Yang, Z.; Magull, J.; Roesky, H. W.; Schmidt, H.-G.; Noltemeyer, M. *Organometallics* **2005**, *24*, 6420–6425.

Nineteen resonances are observed at room temperature, consistent with inequivalence of the two adamantyl groups and of the two faces of the diketiminate ligand. No coalescence of peaks is observed in the ^{1}H NMR spectrum up to 112 °C (Figure S-1), suggesting that the conformation observed in the crystal structure is maintained in solution on the NMR time scale.

The N1−N2, N2−N3, and N3−N4 distances in the tetrazene fragment are very similar (1.317(2), 1.334(2), and 1.309(2) Å, respectively). These distances are intermediate between single and double N−N bond lengths, indicating delocalization of the π-electrons. This in turn suggests form **B** in Figure 1, which has no localized double bonds.

Mechanism of Tetrazene Formation. The synthesis of tetrazene complexes from organic azides and low-valent metal precursors is well-precedented.[6−14,17−19] The mechanism is thought to proceed through a transient imidometal intermediate that undergoes a dipolar 1,3-cycloaddition with a second equivalent of azide. Bergman, Andersen, and co-workers have shown that tetrazene complexes can be formed by stoichiometric addition of an organic azide to isolated Zr[20] and Os[21] imido complexes.

In this (β-diketiminato)iron system, we have previously characterized L^{Me}Fe=NAd,[22] the imidoiron (III) species that would be the putative intermediate prior to the cycloaddition. It is metastable, and must be prepared in the presence of 4-*tert*-butylpyridine (tBupy), which is necessary to avoid formation of the hexazene complex $\{L^{Me}Fe\}_2(\mu\text{-}AdN_6Ad)$.[16] As noted above, the addition of tBupy is necessary in the synthesis of **1** for the same reason. To query the capability of the imido complex to form the tetrazene complex, we generated L^{Me}Fe(=NAd) from addition of 2 equiv of N_3Ad (1 equiv per iron) to $L^{Me}FeNNFeL^{Me}$ in the presence of tBupy, and verified that its ^{1}H NMR spectrum was the same as previously reported,[22] with no **1** present. Addition of additional N_3Ad (1 equiv per iron) led to an immediate color change to olive green and formation of **1** in >90% yield, as judged by ^{1}H NMR spectroscopy. Therefore, the imidoiron(III) complex is a kinetically competent intermediate in the formation of the tetrazene complex.

Magnetic Studies. The electronic structure of the tetrazene fragment was evaluated using a variety of spectroscopic techniques. The solution magnetic moment of **1** at room temperature is 4.0(3) μ_B, consistent with a total spin of 3/2. The solid-state magnetic moment at temperatures above 100 K is constant at 4.37 μ_B (Figure 3), close to the solution value. There is a low-temperature decline in $\mu_{eff}(T)$ below 50 K, which indicates the presence of substantial zero-field splitting. We were able to simulate the full temperature dependence of μ_{eff} with an $S = 3/2$ model using $g_{av} = 2.26$ and an axial zero-field splitting parameter $D = -15$ cm^{-1}, where EPR data (described below) gave the sign of D and the rhombicity parameter $E/D \sim 0$.

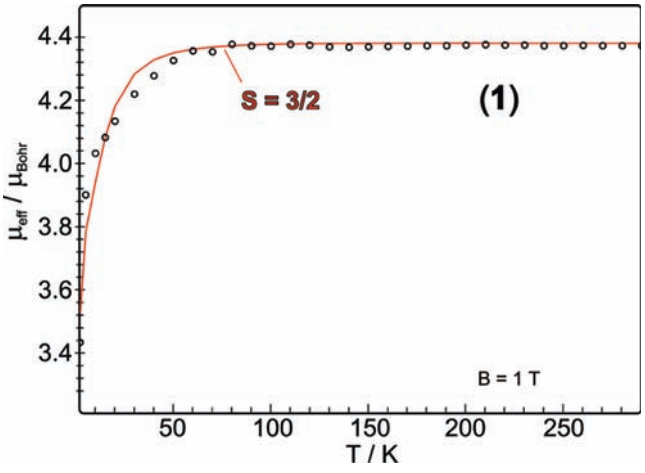

Figure 3. Variable temperature magnetic susceptibility of a solid sample of L^{Me}Fe(AdNNNNAd) (**1**). The data are fit with $S = 3/2$, $g_{av} = 2.26$, and $D = -15$ cm^{-1} (red line).

The X-band EPR derivative spectrum of a frozen solution of **1** at 8 K (Figure 4, bottom) shows a single sharp low-field peak at $g_{eff} = 7.6$. The spectrum appears somewhat noisy because of the small intensity of the signal, as discussed in more detail below. The position of the low-field peak is similar to sharp signals in another (β-diketiminato)iron species with $S = 3/2$, the iron(I) complex L^{Me}Fe(HCCPh).[23] In L^{Me}Fe(HCCPh), the electronic structure was dominated by the contribution of first-order orbital momentum. Here, the situation is different: we can explain the spectrum of **1** by usual zero-field splitting of the spin quartet.[24]

Zero-field splitting of the $S = 3/2$ quartet yields two separate Kramers doublets, $|m_S\rangle = |\pm 1/2\rangle$ and $|\pm 3/2\rangle$. Since the splitting by $2D$ is large compared to the microwave quantum energy ($h\nu \approx 0.3$ cm^{-1}), X-band resonances occur only within the doublets. Thus, the EPR spectrum is a superposition of two subspectra that can be described by two independent fictitious spins $S' = 1/2$ with *effective* g tensors $\mathbf{g}'^{\pm 1/2}$ and $\mathbf{g}'^{\pm 3/2}$. For sufficiently large zero-field splitting the effective g' values, which can be directly read off the spectrum, depend only on the rhombicity E/D and the **g** tensor of the system spin $S = 3/2$ (cf. Supporting Information, Figure S-5).[24] In this model the dominant EPR line of **1** can be assigned as the $g'_z{}^{\pm 3/2}$ resonance of the very anisotropic $|\pm 3/2\rangle$ Kramers doublet, which for $E/D \approx 0$ and isotropic $g = 2$ has effective g values $g'_{x,y}{}^{\pm 3/2} \sim 0$, $g'_z{}^{\pm 3/2} = 6$ (see Supporting Information, Figure S-5). Since the observed g' value, however, is considerably higher than $g'_z{}^{\pm 3/2} = 6$, we can infer that the electronic **g** tensor for $S = 3/2$ has a z-component larger than 2. A reasonable value of $g_z = 2.6$ reproduces the position of the experimentally observed EPR signal at $g' = 7.6$.

(19) Trogler, W. C.; Johnson, C. E.; Ellis, D. E. *Inorg. Chem.* **1981**, *20*, 980–986.
(20) Meyer, K. E.; Walsh, P. J.; Bergman, R. G. *J. Am. Chem. Soc.* **1995**, *117*, 974–985.
(21) Michelman, R. I.; Bergman, R. G.; Andersen, R. A. *Organometallics* **1993**, *12*, 2741–2751.
(22) Eckert, N. A.; Vaddadi, S.; Stoian, S.; Lachicotte, R. J.; Cundari, T. R.; Holland, P. L. *Angew. Chem., Int. Ed.* **2006**, *45*, 6868–6871.
(23) Stoian, S. A.; Yu, Y.; Smith, J. M.; Holland, P. L.; Bominaar, E. L.; Münck, E. *Inorg. Chem.* **2005**, *44*, 4915–4922.
(24) Palmer, G. Electron Paramagnetic Resonance of Metalloproteins. In *Physical Methods in Bioinorganic Chemistry*; Que, L., Jr., Ed.; University Science Books: Sausalito, CA, 2000.

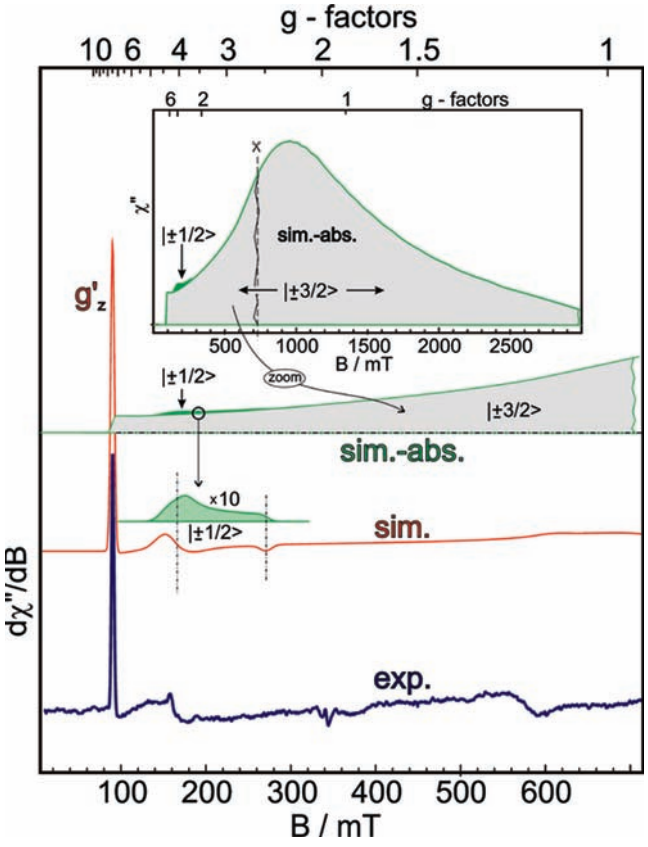

Figure 4. Derivative X-band EPR spectrum of $L^{Me}Fe(AdNNNNAd)$ (**1**) in a frozen toluene glass at 8 K ("exp") and spin-Hamiltonian simulation with $S = 3/2$ ("sim") using $D = -16$ cm^{-1}, $E/D = 0.06$, $\sigma(E/D) = 0.04$, $\mathbf{g} = (2.07, 2.07, 2.6)$. The shaded green curves show the simulated absorption spectrum, which extends to extremely high field. The contributions of the two zero-field split Kramers doublets are labeled as $|\pm1/2\rangle$ and $|\pm3/2\rangle$, respectively.

The amplitude of the experimental EPR spectrum is remarkably small, as is evident from the high noise level and apparent baseline distortions in the spectrum. This is because the observed $g'_z{}^{\pm3/2}$ derivative peak accounts only for the onset of an exceedingly broad absorbance spectrum that extends up to very high fields, as shown in the simulated absorption spectrum (inset of Figure 4). The major part of the spectrum is beyond the limits of usual spectrometers (the limiting g' values for $E/D = 0$ would be $g'_{x,y}{}^{\pm3/2} \sim 0$, Supporting Information, Figure S-5). However, the spectrum shows clearly that the resonance doublet $|\pm3/2\rangle$ is the ground state, because the typical subspectrum of the $|\pm1/2\rangle$ doublet with $\mathbf{g}'^{\pm1/2} = (4, 4, 2)$ is hardly observable at 8 K. This means that the zero-field splitting is large and negative, $D < 0$. The spin-Hamiltonian simulation of the derivative spectrum with $S = 3/2$, $D = -16$ cm^{-1}, $E/D = 0.06$, and $\mathbf{g} = (2.07, 2.07, 2.6)$ is shown as the red trace in Figure 4. Importantly, the values used in this simulation are the same as those in the simulation of the magnetic susceptibility of solid **1**.[25]

(25) On the basis of the average **g** value obtained from the magnetic susceptibility data ($g_{av} = 2.26$), we can estimate the other components of the **g** matrix by using the relation $g_{av} = [(g_x^2 + g_y^2 + g_z^2)/3]^{1/2}$. Adopting axial symmetry, we obtain $g = (2.07, 2.07, 2.6)$ for the main components.

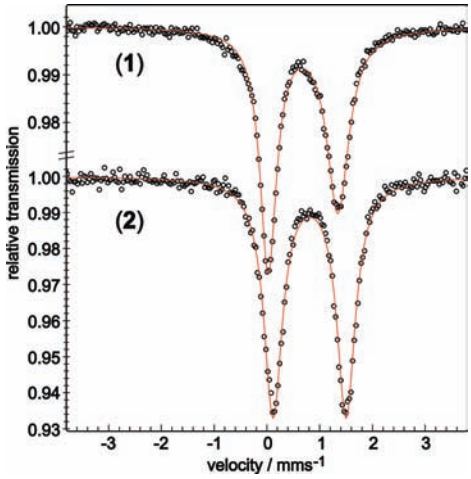

Figure 5. Mössbauer spectra of solid $L^{Me}Fe(AdNNNNAd)$ (**1**) and [K(cryptand-222)][$L^{Me}Fe(AdNNNNAd)$] (**2**) at 80 K. (Compound **2** is discussed in detail later in the paper.) The solid lines show fits to the data: **1**, $\delta = 0.69(2)$ mm/s and $\Delta E_Q = 1.32(4)$ mm/s; **2**, $\delta = 0.81(2)$ mm/s and $\Delta E_Q = 1.40(2)$ mm/s.

The simulation indicates also that the expected contribution of the excited state $|\pm1/2\rangle$ may be blurred by the effects of micro-heterogeneity of **1** in the frozen solution. As is evident in the rhombogram for $S = 3/2$ systems (Supporting Information, Figure S-5), a Gaussian distribution of the rhombicity E/D with $\sigma(E/D) = 0.03$ broadens the $|\pm1/2\rangle$ signals much more than the $|\pm3/2\rangle$ signals. Because of the weakness of the data, it is not possible to assign the extremely small feature at $g \sim 4$, but these considerations indicate clearly that a distribution in E/D of 0.03 or more would rationalize the absence of a clearly discernible $|\pm1/2\rangle$ signal.

Mössbauer Spectroscopy. The zero-field Mössbauer spectrum of solid **1** (Figure 5, top) recorded at 80 K fits to a doublet with $\delta = 0.69(2)$ mm/s and $\Delta E_Q = 1.32(4)$ mm/s. The lines are asymmetrically broadened. Since the effect decreases with increasing temperature (see Supporting Information, Figure S-3 for a spectrum taken at 180 K), we can explain this as intermediate spin relaxation, where the relaxation time of the electronic spin at 80 K approaches the regime of the nuclear Larmor precession.[26]

The isomer shift and quadrupole splitting of **1** are consistent with high-spin iron(II). For example, we have observed δ values of 0.48−0.90 mm/s in other iron(II) diketiminate complexes.[27] A similar value of $\delta = 0.55$ mm/s has been seen in a four-coordinate iron(II) complex supported by a tris(phosphino)borate ligand,[28] while a larger value of $\delta = 0.96$ mm/s was seen for an iron(II) complex of a tris(thioether)borate.[14] Tetrahedral iron(II) ions in iron−sulfur clusters give $\delta = 0.60$−0.70 mm/s.[12,29] High-spin iron(III) complexes give much smaller δ values, and so we can rule

(26) Gütlich, P.; Link, R.; Trautwein, A. *Mössbauer Spectroscopy and Transition Metal Chemistry*; Springer Verlag: Berlin, 1978.
(27) Andres, H.; Bominaar, E. L.; Smith, J. M.; Eckert, N. A.; Holland, P. L.; Münck, E. *J. Am. Chem. Soc.* **2002**, *124*, 3012–3025.
(28) Hendrich, M. P.; Gunderson, W.; Behan, R. K.; Green, M. T.; Mehn, M. P.; Betley, T. A.; Lu, C. C.; Peters, J. C. *Proc. Natl. Acad. Sci. U.S.A.* **2006**, *103*, 17107–17112.
(29) (a) Beinert, H.; Holm, R. H.; Münck, E. *Science* **1997**, *277*, 653–659. (b) Schünemann, V.; Winkler, H. *Rep. Prog. Phys.* **2000**, *63*, 263–353.

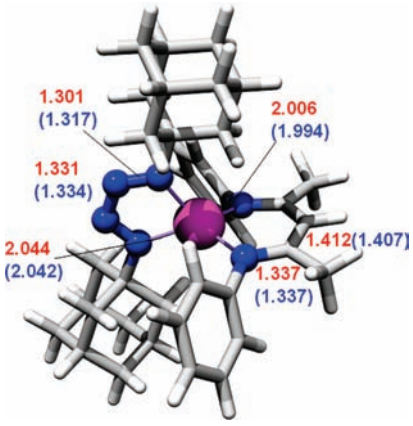

Figure 6. Optimized structure of **1** from DFT computations. Numbers in red are bond lengths [Å] from the optimized geometry, and blue numbers in parentheses are those from the experimental X-ray crystal structure.

out form **C** (Fe^{3+} with tetrazene dianion).[12] On the other hand, a high-spin iron(I) formulation (form **A**) is not ruled out by the Mössbauer data, because of the small number of well-characterized high-spin iron(I) complexes.[23]

Density-Functional Computations. At this point, form **B** (Figure 1) rationalizes all of the data for **1**. Antiferromagnetic coupling of a high-spin ferrous ion with a radical tetrazene ligand would give an overall spin state of $S = (2 - 1/2) = 3/2$, consistent with the magnetic and EPR data. Form **A** (an iron(I) complex with a neutral tetrazene ligand) is inconsistent with the N−N bond lengths in the crystal structure but possibly compatible with the spectroscopic data.

To obtain more insight into the electronic structure of **1**, scalar relativistic density-functional theory (DFT) calculations were performed at the B3LYP[30]/DKH2 level of theory[31] using broken-symmetry methods[32] and a relativistically recontracted[33] basis set (def2-TZVP[34] on Fe and N, SV(P)[35] on other atoms). The full adamantyl groups were included in the model, but the isopropyl groups of the diketiminate ligand were omitted. The overall quartet spin state was used, but no other assumptions were made about the distribution of electrons. The optimized structure is shown in Figure 6, which highlights the agreement between the experimental bond lengths and the optimized metrical parameters from the computations. The Mössbauer parameters were also predicted from the quantum-chemical model as a check of its accuracy. The calculated isomer shift ($\delta = 0.65$ mm/s) is in good agreement with the observed value ($\delta = 0.69(2)$ mm/s), while the calculated quadrupole splitting ($\Delta E_Q = 2.04$ mm/s) deviates somewhat from the experimental value ($\Delta E_Q = 1.32(4)$ mm/s). Note that the isomer shift is generally predicted more accurately by DFT calculations, and the deviation of 0.7 mm/s in quadrupole splitting is within the range expected for complexes of low symmetry.[36,37]

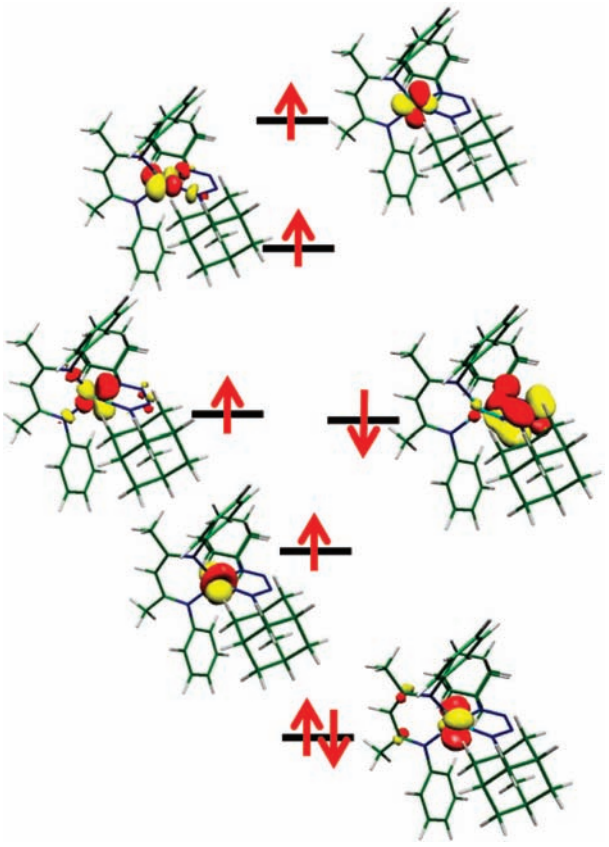

Figure 7. Qualitative MO scheme of the spectroscopically and structurally validated model of **1**, showing opposite spins on a high-spin Fe(II) ion and a tetrazene anion radical.

Figure 7 shows a qualitative MO diagram corresponding to this optimized solution. As explained elsewhere,[38] one can make use of the so-called corresponding orbital transformation to transform the spin-unrestricted broken symmetry solution into a more illuminating display. In this representation the spin-up and spin-down orbitals do not have a well-defined energy, but instead for each spin-up orbital there is at most one spin-down orbital that has a nonzero spatial overlap with the spin-up orbital. Thus, the occupied orbitals are ordered into essentially doubly occupied MOs (spatial overlap >0.99), spin-coupled pairs (overlap significantly smaller than 1) and "unmatched" singly occupied orbitals.[38,39] As has become common practice in many studies of metal-radical systems,[4,38] we use quasi-restricted orbitals to represent doubly occupied and empty MOs and use the unrestricted

(30) (a) Becke, A. D. *Phys. Rev. A* **1988**, *38*, 3098–3100. (b) Becke, A. D. *J. Chem. Phys.* **1993**, *98*, 1372–1377. (c) Lee, C. T.; Yang, W. T.; Parr, R. G. *Phys. Rev. B* **1988**, *37*, 785–789.

(31) Neese, F.; Becker, U.; Ganyushin, D.; Liakos, D.; Kossmann, S.; Petrenko, T.; Riplinger, C.; Wennmohs, F. *ORCA − an ab initio, density functional and semiempirical program package*, Version 2.6, revision 71; Universität Bonn: Bonn, Germany, 2008.

(32) Noodleman, L. *J. Chem. Phys.* **1981**, *74*, 5737–5743.

(33) Pantazis, D. A.; Chen, X.-Y.; Landis, C. R.; Neese, F. *J. Chem. Theor. Comp.* **2008**, *4*, 908–919.

(34) (a) Weigend, F.; Ahlrichs, R. *Phys. Chem. Chem. Phys.* **2005**, *7*, 3297–3305. (b) Schäfer, A.; Huber, C.; Ahlrichs, R. *J. Chem. Phys.* **1994**, *100*, 5829–5835.

(35) Schäfer, A.; Horn, H.; Ahlrichs, R. *J. Chem. Phys.* **1992**, *97*, 2571–2577.

(36) Römelt, M.; Ye, S.; Neese, F. *Inorg. Chem.* **2009**, *48*, 784–785.

(37) Calculated Mössbauer isomer shifts are typically within 0.1 mm/s, and prediction of quadrupole splitting values is less reliable. See: Neese, F. *Coord. Chem. Rev.* **2009**, *253*, 526–563.

(38) (a) Neese, F. *J. Phys. Chem. Solids* **2004**, *65*, 781–785. (b) Herebian, D.; Wieghardt, K.; Neese, F. *J. Am. Chem. Soc.* **2003**, *125*, 10997–11005.

(39) Kirchner, B.; Wennmohs, F.; Ye, S.; Neese, F. *Curr. Opin. Chem. Biol.* **2007**, *11*, 134–141.

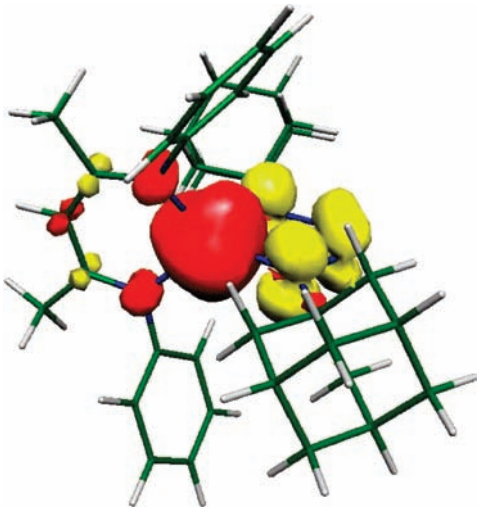

Figure 8. Spin-density plot of compound **1**. "Up" and "down" spins are shown in orange and yellow, respectively.

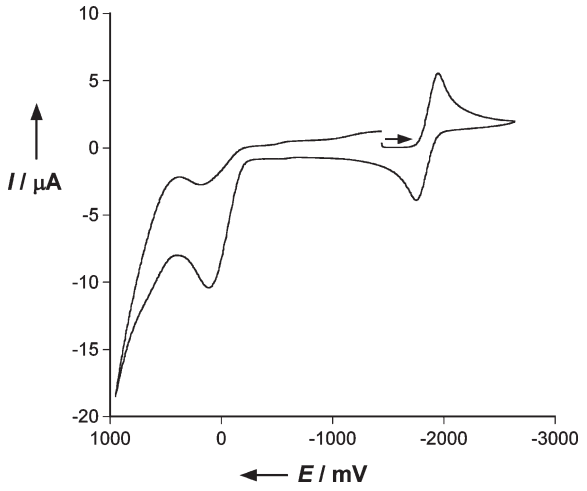

Figure 9. Cyclic voltammogram of a 2.2 mM solution of $L^{Me}Fe(AdNNNNAd)$ (**1**) in THF with 0.15 M $[^nBu_4N][PF_6]$ supporting electrolyte. Potentials are relative to the $Cp_2Fe^{+/0}$ couple (0 V), with more reducing potentials to the right. Scan rate: 500 mV s^{-1}. See Supporting Information, Figure S-2 for electrochemistry details.

Scheme 2. Synthesis of the Reduced Tetrazene Complex **2**

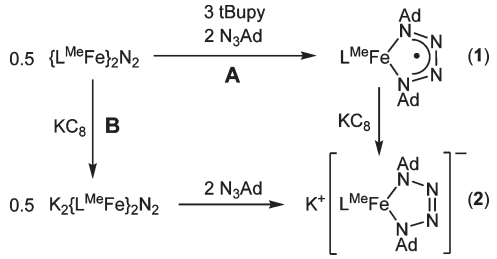

corresponding orbitals to display spin-coupled electron pairs. Such MO schemes are necessarily qualitative since the MOs that are involved do not have a well-defined orbital energy, but they provide significant insight into the bonding.

Figure 7 shows the magnetic orbitals arising from this analysis. There are three unpaired electrons localized on the central iron, and one doubly occupied MO is essentially a nonbonding iron 3d orbital. Importantly, there is one spin-coupled pair that is composed of a spin-up iron 3d-based orbital and a spin-down tetrazene-based π^*-orbital. Figure 8 illustrates the total spin density, showing that the spins on the metal and ligand are opposite. The magnetic orbital overlap is $S = 0.544$ and the calculated J value is -850 cm^{-1},[40] indicating strong metal−ligand antiferromagnetic coupling. Therefore, the spectroscopically and structurally validated DFT model demonstrates that **1** is a high-spin iron(II) complex with strong antiferromagnetic coupling to a tetrazene radical anion. This interpretation is consistent with all of the experimental data.

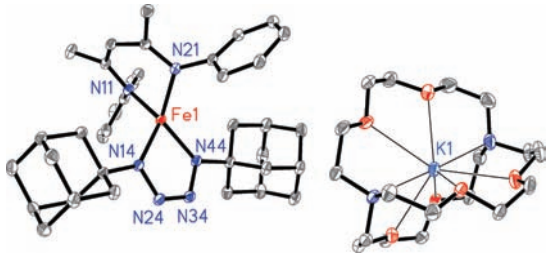

Figure 10. Molecular structure of $[K(cryptand\text{-}222)][L^{Me}Fe(AdNNNNAd)]$ (**2**), using 50% probability thermal ellipsoids. Hydrogen atoms and isopropyl groups on the diketiminate ligand are removed for clarity. Selected bond distances [Å]: Fe1−N14, 2.0089(7); Fe1−N44, 1.9556(8); N14−N24, 1.371(1); N24−N34, 1.282(1); N34−N44, 1.380 (1); Fe1−N11, 2.0689(7); Fe1−N21, 2.0665(8).

Reduction of the Radical Tetrazene to an Anionic Tetrazene. To learn about the redox behavior of the tetrazene complex, we investigated the reduction of **1**. Cyclic voltammetry of a tetrahydrofuran (THF) solution of **1** reveals several features. First, an irreversible feature is visible with $E_{pa} = +0.12$ V versus the ferrocene/ferrocenium couple (Figure 9), although this is partially obscured by the imminent solvent oxidation wave. Consistent with the irreversibility of this oxidation wave, we have not been able to isolate the one-electron oxidized form of **1** since addition of oxidants such as $[Cp_2Fe][BAr^F_4]$ or AgOTf to a solution of **1** invariably led to decomposition. Additionally, the voltammogram shows a reversible one-electron reduction at -1.84 V (versus $Cp_2Fe^{+/0}$). Chemical reduction of **1** was achieved through addition of KC_8 to a solution of **1** (Scheme 2, Route A) in 83% yield. The ^1H NMR spectrum of the resulting solution indicates complete consumption of **1** and the appearance of a new paramagnetic species. The same species is also accessible by addition of 4 equiv of N_3Ad (2 equiv per iron) to a solution of the iron(0) synthon $K_2[L^{Me}FeNNFeL^{Me}]$[15] (Scheme 2, Route B). Addition of 1 equiv of cryptand-222 to this species affords X-ray quality crystals of the reduced complex $[K(cryptand\text{-}222)][L^{Me}Fe(AdNNNNAd)]$ (**2**) (Figure 10). Like **1**, compound **2** has pseudo-C_s symmetry in the solid state, and the 22 peaks in the ^1H NMR spectrum are consistent with this symmetry in solution.

(40) Calculation of the exchange coupling used $J = -(E_{HS} - E_{BS})/(\langle S^2\rangle_{HS} - \langle S^2\rangle_{BS})$ according to the Yamaguchi formalism. For details, see: Yamaguchi, K.; Takahara, Y.; Fueno, T. In *Applied Quantum Chemistry*; Smith, V. H., Ed.; Reidel: Dordrecht, 1986; p 155.

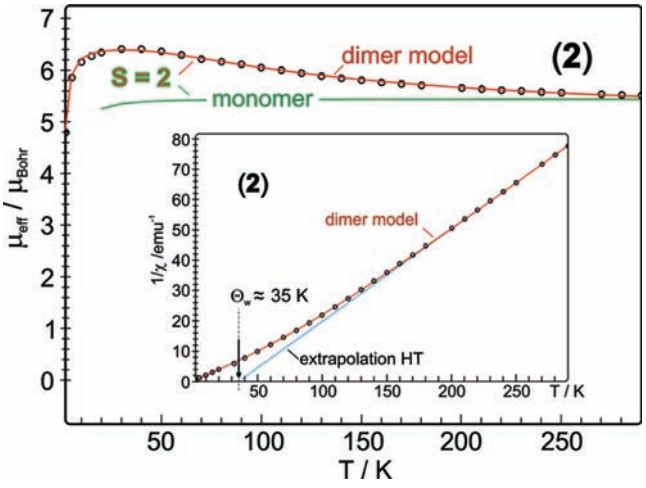

Figure 11. Temperature dependence of the effective magnetic moment μ_{eff} of a solid sample of [K(cryptand-222)][L^{Me}Fe(AdNNNNAd)] (**2**). The solid red line through the data is a simulation, assuming ferromagnetic spin coupling between pairs of adjacent molecules with spins $S_1 = S_2 = 2$ (dimer model). The parameters are $g_{av,i} = 2.04$, $D_i = 6.0\ cm^{-1}$ for the identical iron centers and $J' = +10.3\ cm^{-1}$ for the pairwise intermolecular coupling. (Experimental and simulated values are given per one iron center.) The green line represents a fit to the high temperature limit of the data by a monomer approach with $S = 2$, $g_{av} = 2.22$, and $D = -8\ cm^{-1}$ (arbitrarily fixed). Inset: Plot of the inverse of the molar susceptibility versus temperature. The dashed blue line is a linear extrapolation of the high-temperature branch to estimate the Curie−Weiss temperature ($\Theta_W \approx 35$ K).[43]

The large change in N−N bond lengths upon reduction is noteworthy. The central N−N distance has decreased by 0.052(2) Å to that of a double bond at 1.282(1) Å,[41] and the other N−N bond lengths have lengthened by 0.06 Å. This "long-short-long" configuration of N−N bonds strongly suggests form **C** for the reduced complex, which implies a dianionic Ad_2N_4 ligand and iron(II).

The Mössbauer spectrum of **2** (Figure 5) shows $\delta = 0.81(2)$ mm/s and $\Delta E_Q = 1.40(2)$ mm/s, values that are again consistent with high-spin iron(II) or high-spin iron(I) but are similar to those in compound **1**. The solid-state effective magnetic moment of **2** is temperature dependent, whereas the data asymptotically approach the value $\approx 5.4\ \mu_B$ at 300 K (Figure 11), similar to the magnetic moment measured in THF solution at 25 °C (4.8(2) μ_B). The high-temperature range of $\mu_{eff}(T)$ is consistent with an $S = 2$ model with $g_{av} = 2.22$, though the simulation deviates from experimental at low temperature (Figure 11, green line labeled "monomer"). The faint maximum of the experimental data (at about 20 K) is characteristic of ferromagnetic coupling,[42] for which we can invoke only intermolecular interactions. An approximation of this solid state effect by using a dimer model, in which the unknown coupling schemes in the solid are replaced by the interaction of pairs of identical molecules with spin $S_i = 2$, yields an excellent fit with a coupling constant $J' = +10.3\ cm^{-1}$ (Figure 11, red line labeled "dimer model"). The presence of an intermolecular interaction between spin-quintet molecules (in contrast to an impurity, for instance) is further supported by a plot of $1/\chi(T)$ versus T. At high temperatures the curve is linear and the slope clearly reveals $S = 2$,[43] whereas the extrapolation to large $\chi(T)$ at low temperature yields an alternative estimate of the ferromagnetic coupling in terms of the Curie−Weiss temperature Θ_W, which is roughly 35 K.[44] We speculate that the intermolecular magnetic interaction is mediated by the diketiminate ligand backbones, because there is a close (3.74 Å) intermolecular contact between adjacent diketiminates that is evident in the solid-state structure of **2**. Although further study is clearly needed to identify the nature of the intermolecular interaction, there is no doubt that the ground-state of **2** is a quintet.

We now move to the search for the best description of the electronic structure of **2** in terms of the resonance structures in Figure 1. The $S = 2$ ground-state is inconsistent with form **A**, because a high-spin iron(0) with diamagnetic ligands would have $S = 1$. The magnetic susceptibility data are difficult to rationalize using form **B** because this model would require extremely strong ferromagnetic coupling ($> +250\ cm^{-1}$) between a high-spin iron(I) ion and the radical ligand to generate a sufficiently isolated $S = 2$ ground-state to exhibit the observed constant effective moment above 200 K. Therefore, the Mössbauer and magnetic data most strongly suggest that **2** is a high spin iron(II) center coordinated to a diamagnetic, dianionic tetrazene fragment (form **C**). This interpretation is most consistent with the N−N bond lengths in the X-ray crystal structure as well.

DFT calculations on the reduced species gave metrical parameters consistent with the X-ray crystal structure, including the contraction of the central N−N bond (Supporting Information, Figure S-6). Also in agreement with experiment, the lowest energy electronic state has a total spin of $S = 2$ and consists of a high-spin Fe(II) ion coordinated to a tetrazene ligand with little spin density (Supporting Information, Figure S-6). The calculated isomer shift ($\delta = 0.72$ mm/s) is in reasonable agreement with the experimental isomer shift ($\delta = 0.81$ mm/s) but the deviation is on the upper end of the employed methodology.[45] Unfortunately, no calculation that we performed matched the experimentally found quadrupole splitting: the calculated values of ΔE_Q are much too high (> 4 mm/s). Given this caveat, the computational results are also consistent with ligand-centered reduction chemistry upon going from **1** to **2**.

Conclusion

A neutral iron-tetrazene complex L^{Me}Fe(AdNNNNAd) (**1**) has been synthesized from an iron(I) precursor and an

(41) The average N=N bond length of XN=NX (X = nonmetal) is 1.28(4) Å, calculated from 3041 examples in the Cambridge Structural Database (Aug 2008 update). Allen, F. H. *Acta Crystallogr.* **2002**, *B58*, 380–388.

(42) Girerd, J. J.; Journaux, Y., Molecular Magnetism in Bioinorganic Chemistry. In *Physical Methods in Bioinorganic Chemistry*; Que, L., Ed.; University Science Books: Sausalito, CA, 2000; pp 321−374.

(43) Kahn, O. *Molecular Magnetism*; VCH Publishers, Inc.: Weinheim, Germany, 1993.

(44) The Curie−Weiss temperature is related to the strength J of the intermolecular coupling as: $\Theta_W = zJ\,S(S+1)/3k$, where z is the number of coupled nearest neighbors, S is the spin, and k is the Boltzmann constant (see ref 43). Substituting $z = 6$, $S = 2$, $k = 0.69\ cm^{-1}/K$, we find $J = 2\ cm^{-1}$. A similar result is obtained ($J = 1.7\ cm^{-1}$) if we reassign the value $J' = 10\ cm^{-1}$ from the dimer model used above to six coupling paths per iron center, instead of two in the basic model.

(45) (a) Neese, F. *Inorg. Chim. Acta* **2002**, *337*, 181–192. (b) Sinnecker, S.; Slep, L. D.; Bill, E.; Neese, F. *Inorg. Chem.* **2005**, *44*, 2245–2254.

organic azide. An imidoiron(III) species is a kinetically competent intermediate in the reaction. This work represents the first combined spectroscopic, magnetic, and computational characterization that clearly indicates a monoanionic radical tetrazene ligand ($AdNNNNAd^{\bullet-}$). In this iron complex, the unpaired spin on the tetrazene is strongly antiferromagnetically coupled to a high spin iron(II) center to give a ground state of $2 - 1/2 = 3/2$. The radical tetrazene fragment is stable enough to be cleanly and reversibly reduced to a dianionic tetrazene ligand ($AdNNNNAd^{2-}$) without a change in the oxidation state of the metal. Therefore, the tetrazene fragment shows promise as a useful redox-active ligand in other synthetic studies.

Experimental Section

General Considerations. All manipulations were performed under a nitrogen atmosphere in an MBraun glovebox maintained at or below 1 ppm of O_2 and H_2O. 1-Azidoadamantane was purchased from Aldrich and crystallized twice from pentane prior to use. *tert*-Butylpyridine was vacuum distilled from calcium hydride and stored over 3Å molecular sieves (activated at >300 °C for 12 h under vacuum). Cryptand-222 was purchased from Aldrich and used as received. The compound $L^{Me}FeNNFeL^{Me}$ was prepared as previously described.[15] Pentane, diethyl ether, THF, and toluene were purified by passage through activated alumina and "deoxygenizer" columns from Glass Contour Co. (Laguna Beach, CA, U.S.A.). Before use, an aliquot of each solvent was tested with a drop of sodium benzophenone ketyl in THF. C_6D_6 was dried over activated alumina, and THF-d_8 was vacuum transferred from a purple sodium benzophenone ketyl. Celite was dried at 200 °C overnight under vacuum. All glassware was dried overnight at 150 °C. NMR data were collected on either a Bruker Avance 400 or Bruker Avance 500 spectrometer, and spectra are referenced to residual C_6D_5H (δ 7.16 ppm) or C_4D_7HO (δ 3.58 ppm). The NMR probe temperature for the variable-temperature measurements was calibrated using ethylene glycol.[46] IR data were recorded on a Shimadzu 8400S spectrometer using KBr pellets. UV−vis spectra were recorded on a Cary 50 spectrometer using screw-cap cuvettes. CV measurements were obtained using a Cypress Systems 3100 potentiostat. The working electrode was Pt with a 1 mm diameter working area, and Ag wires were used as auxiliary and reference electrodes. All measurements were referenced with a ferrocene standard, and reported relative to the Cp_2Fe^+/Cp_2Fe couple (0 V). Elemental analysis was determined by Columbia Analytical Services (previously Desert Analytics). Room temperature solution magnetic susceptibilities were determined by the Evans method.[47]

L^{Me}Fe(AdNNNNAd) (1). To a stirring solution of L^{Me}-$FeNNFeL^{Me}$ (260 mg, 0.267 mmol) in pentane (5 mL) was added 4-*tert*-butylpyridine (0.24 mL, 1.6 mmol, 6 equiv), which caused a color change from dark red to dark blue. The solution was stirred for 10 min, and a solution of 1-adamantyl azide (190 mg, 1.06 mmol, 4 equiv) in pentane (1 mL) was added dropwise over ~30 s. Effervescence was observed, concomitant with a color change to red-orange, then to dark green. After 12 h, the dark mixture was cooled to −45 °C, and a dark olive-green solid was collected on a fritted glass funnel. The solid was washed with cold pentane (−45 °C, 3 × 5 mL) and dried under vacuum to afford L^{Me}Fe(AdNNNNAd) (345 mg, 81%). X-ray quality crystals were obtained from a saturated diethyl ether solution cooled to −45 °C. ^{1}H NMR (500 MHz, C_6D_6): δ 91 (2H), 29 (6H), 12 (2H), 3.0 (6H), 0.9 (6H), −1.3 (2H), −3.4 (3H), −4.6 (3H), −7.6 (6H), −8.7 (3H), −12 (3H), −13 (6H), −17 (6H), −18 (2H), −26 (3H), −31 (3H), −32 (6H), −64 (1H), −107 (2H) ppm. Variable-temperature ^{1}H NMR spectra are shown in the Supporting Information, Figure S-1. IR: 3055(w), 2964(m), 2907(s), 2868(m), 2849(m), 1508(s), 1460(m), 1439(m), 1381(s), 1315(m), 1259(m), 1169(m), 1097(m), 1016(m), 933(w), 795(m), 760(w) cm^{-1}. UV−vis (toluene): λ (nm), ε (cm^{-1} mM^{-1}): 420 (6.0), 460 (sh, ~3), 591 (1.1), 855 (0.1). μ_{eff} (C_6D_6, 25 °C): 4.0(3) μ_B. Anal. Calcd for $C_{49}H_{71}N_6Fe$ (FW = 800.0): C, 73.57; H, 8.95; N, 10.51. Found: C, 74.48; H, 8.67; N, 10.37.

[K(cryptand-222)][L^{Me}Fe(AdNNNNAd)] (2). A vial was loaded with L^{Me}Fe(AdNNNNAd) (157 mg, 0.196 mmol) and KC_8 (32 mg, 0.24 mmol, 1.2 equiv). Pentane (5 mL) was added, and the slurry was stirred for 18 h. The mixture was filtered through Celite and dried to a dark red solid. The solid was suspended in THF (3 mL), and a solution of cryptand-222 (77 mg, 0.21 mmol, 1.1 equiv) in THF (1 mL) was added, affording a dark green solution. The solution was layered with pentane (10 mL), and dark green crystals of [K(cryptand-222)][L^{Me}Fe(AdNNNNAd)] were obtained upon cooling to −45 °C (198 mg, 83%). ^{1}H NMR (500 MHz, THF-d_8): δ 105 (2H), 36 (6H), 12 (2H), 9.5 (6H), 9.0 (12H), 8.7 (12H), 6.3 (12H), 1.3 (2H), −0.4 (6H), −1.1 (3H), −11 (3H), −12 (6H), −12 (3H), −15 (3H), −18 (3H), −22 (6H), −23 (2H), −29 (2H), −32 (1H), −55 (6H), −63 (6H), −137 (2H). IR: 3060 (w), 2959 (s), 2894 (s), 2840 (s), 2816 (m), 1507 (m), 1458 (m), 1433 (m), 1392 (s), 1355 (m), 1319 (m), 1302 (m), 1260 (m), 1171 (m), 1133 (m), 1105 (s), 1080 (m) cm^{-1}. UV−vis (THF): λ (nm), ε (cm^{-1} mM^{-1}): 349 (16), 415 (sh, ~4), 650 (0.80), 620 (sh, ~0.77). μ_{eff} (THF-d_8, 25 °C): 4.8(2) μ_B. Anal. Calcd for $C_{67}H_{107}N_8O_6FeK$ (FW = 1215.6): C, 66.20; H, 8.87; N, 9.22. Found: C, 61.32; H, 7.95; N, 6.55. Despite repeated attempts, we were not able to obtain satisfactory elemental analysis results on this highly air-sensitive compound. Note, however, that the Mössbauer spectrum of **2** indicates high purity of iron-containing components.

Crystallography. Crystals were placed onto the tip of a 0.1 mm diameter glass capillary tube or fiber and mounted on a Bruker SMART APEX II CCD Platform diffractometer[48] for a data collection at 100(1) K using Mo Kα radiation and a graphite monochromator. A randomly oriented region of reciprocal space was surveyed: four major sections of frames were collected with 0.50° steps in ω at four different ϕ settings and a detector position of −33° in 2θ. The intensity data were corrected for absorption.[49] Final cell constants were calculated from the *xyz* centroids of >3750 strong reflections from the actual data collection. The structures were solved using SHELXS-97[50] and refined using SHELXL-97.[50] The space groups $P2_1/n$ (**1**) and $P\bar{1}$ (**2**) were each determined based on systematic absences and intensity statistics. All non-hydrogen atoms were refined with anisotropic displacement parameters. All hydrogen atoms were placed in ideal positions and refined as riding atoms with relative isotropic displacement parameters. In the structure of **1**, there is one co-crystallized diethyl ether molecule per iron. One isopropyl group was modeled as disordered over two positions (70:30). In **2**, highly disordered co-crystallized solvent (THF and/or pentane) was present that could not be modeled satisfactorily. The reflection contributions from the solvent were removed using program PLATON, function SQUEEZE,[51] which determined there to be 87 electrons in

(46) (a) Ammann, C.; Meier, P.; Merbach, A. E. *J. Magn. Reson.* **1982**, *46*, 319–321. (b) Kaplan, M. L.; Bovey, F. A.; Cheng, H. N. *Anal. Chem.* **1975**, *47*, 1703−1705.

(47) (a) Baker, M. V.; Field, L. D.; Hambley, T. W. *Inorg. Chem.* **1988**, *27*, 2872–2876. (b) Schubert, E. M. *J. Chem. Educ.* **1992**, *69*, 62.

(48) *APEX2*, V2.2−0; Bruker Analytical X-ray Systems: Madison, WI, 2007.

(49) *SADABS V2.10*, Blessing, R. *Acta Crystallogr.* **1995**, *A51*, 33–38.

(50) Sheldrick, G. M. *Acta Crystallogr.* **2008**, *A64*, 112–122.

(51) Spek, A. L. *PLATON: A multipurpose crystallographic tool*, version 300106; Utrecht University: Utrecht, The Netherlands, 2006.

743 Å^3 removed per unit cell. The final full matrix least-squares refinement for **1** converged to $R1 = 0.0528$ (F^2, $I > 2\sigma(I)$) and $wR2 = 0.1312$ (F^2, all data), and for **2** converged to $R1 = 0.0412$ (F^2, $I > 2\sigma(I)$) and $wR2 = 0.1113$ (F^2, all data). Full crystallographic details are given in the Supporting Information.

Mössbauer Spectroscopy. Mössbauer data were recorded on a spectrometer with alternating constant acceleration. The minimum experimental line width was 0.24 mm/s (full width at half-height). The sample temperature was maintained constant in an Oxford Instruments Variox cryostat. The γ-source was about 0.6 GBq ^{57}Co/Rh. Isomer shifts are quoted relative to iron metal at 300 K. The zero-field spectra were simulated by using Lorentzian doublets.

Magnetic Susceptibility Measurements. Magnetic susceptibility data were measured from powder samples of solid material in the temperature range 2−300 K by using a SQUID susceptometer (MPMS-7, Quantum Design) with a field of 1.0 T. The experimental data were corrected for underlying diamagnetism by use of tabulated Pascal's constants. The susceptibility data, $\chi_T(T)$ or $\mu_{\text{eff}}(T)$, were simulated with our package julX for exchange coupled systems written by E.B.[52] The simulations are based on the usual spin-Hamilton operator for monomeric compounds with zero-field splitting:

$$\hat{H} = g_{\text{av}}\mu_{\text{B}}\hat{\vec{S}}\cdot\vec{B} + D[\hat{S}_z^2 - [S(S+1)]/3 + E/D(\hat{S}_x^2 - \hat{S}_y^2)] \quad (1)$$

where g_{av} is the average electronic g value and D and E/D are the axial zero-field splitting and rhombicity parameters. For the approximation of the intermolecular spin coupling observed for compound **2** by the interaction of two spins we doubled the molar mass of the monomer and used the operator for a symmetric dimer of two spin $S_{\text{i}} = 2$:

$$\hat{H} = -2J[\hat{\vec{S}}_1\cdot\hat{\vec{S}}_2] + g_{\text{Fe}}\mu_{\text{B}}(\hat{\vec{S}}_1 + \hat{\vec{S}}_2)\cdot\vec{B} + \sum_{i=1,2} D_{\text{Fe}}[\hat{S}_{i,z}{}^2 - [S(S+1)]/3] \quad (2)$$

where J represents the intermolecular coupling constant. The magnetic moments were obtained in the simulations from the first order derivative of the eigenvalues of eq 1. Powder summations were done by using a 16-point Lebedev grid.

EPR Spectroscopy. Electron Paramagnetic Resonance spectroscopy used a Bruker ER200D spectrometer interfaced to an IBM PC for data recording. Data acquisition used a locally written program by Prof. Robert Kreilick at the University of Rochester. Spectra were recorded from 50 to 7150 G, and field values were calibrated using samples of known compounds. A field modulation of 15 G and 100 kHz was used. The X-band microwave frequency was 9.422 GHz, and power was nominally 0.3 mW. The time constant was 100 μs. The sample was cooled to 8 ± 3 K using a liquid helium cryostat, and the temperature was calibrated by a thermocouple placed in a sample tube in the cavity.

The spectra were simulated on the basis of the same spin-Hamiltonian description as used for the simulation of the magnetic data (eq 1), except that g_{av} was replaced by a matrix **g** with diagonal components g_x, g_y, g_z. The simulations were performed with our own program ESIM, which was developed from the $S = 5/2$ routines of Gaffney and Silverstone,[53] and which specifically makes use of the calculation of transition fields based on a Newton−Raphson iterative method as described there.

Computations. All calculations reported in this paper were performed with the parallel version of the ORCA program package.[31] We used the B3LYP functional[30] throughout as it has been shown in previous studies[4] to provide correct broken-symmetry solutions where pure GGA functionals fail, and it also reproduces experimental Mössbauer parameters well.[45] We used a relativistically recontracted[33] TZVP[35] basis set for the entire system (91 atoms, 1185 basis functions). Scalar relativistic effects were included in the calculations at the level of the second-order Douglas−Kroll−Hess Hamiltonian.[54] The calculations were significantly accelerated with the recently proposed RIJCOSX algorithm.[55] Unconstrained geometry relaxation was performed in redundant internal coordinates starting from the available crystal structures. Broken-symmetry solutions[32] were generated using the special provisions of the ORCA program and proceed via the localized singly occupied spin-unrestricted natural orbitals of the high-spin solution. Mössbauer parameters were calculated as described previously.[45] Orbital visualization used quasi-restricted orbitals[4,56] and unrestricted corresponding orbitals as described in previous publications.[32] This allows us to obtain a valence-bond display of the calculated electronic structure. The Chimera program was used for visualization.[57]

Acknowledgment. The authors acknowledge financial support from the Petroleum Research Fund (44942-AC to P.L.H.), the U.S. National Science Foundation (Graduate Research Fellowship to R.E.C.), and the University of Bonn and the Max-Planck Society (Fellowship to F.N.). We thank Nick Lees (Northwestern University) for collecting initial EPR data, and thank Bernd Mienert and Andreas Göbels for the Mössbauer and SQUID measurements on very sensitive samples.

Supporting Information Available: Spectroscopic, computational, and crystallographic details. This material is available free of charge via the Internet at http://pubs.acs.org.

(52) Available from: http://ewww.mpi-muelheim.mpg.de/bac/logins/bill/julX_en.php.

(53) Gaffney, B. J.; Silverstone, H. J. Simulation of the EMR Spectra of High-Spin Iron in Proteins. In *Biological Magnetic Resonance*; Berliner, L. J., Reuben, J., Eds.; Plenum Press: New York, 1993; Vol. 13.

(54) Hess, B. A. *Phys. Rev. A* **1986**, *33*, 3742–3748.

(55) Neese, F.; Wennmohs, F.; Hansen, A.; Becker, U. *Chem. Phys.* **2009**, *356*, 98–109.

(56) Schöneboom, J.; Neese, F.; Thiel, W. *J. Am. Chem. Soc.* **2005**, *127*, 5840–5853.

(57) Molecular graphics images were produced using the UCSF Chimera package from the Resource for Biocomputing, Visualization, and Informatics at the University of California, San Francisco (supported by NIH P41 RR-01081). Pettersen, E. F.; Goddard, T. D.; Huang, C. C.; Couch, G. S.; Greenblatt, D. M.; Meng, E. C.; Ferrin, T. E. *J. Comput. Chem.* **2004**, *25*, 1605–1612.